Foams generated from viscous non-Newtonian shear-thinning liquids in a continuous multi rotor-stator device

Jabarkhyl, Saifullah; Barigou, Mostafa; Zhu, Shiping; Rayment, Pip; Lloyd, David M.; Rossetti, Damiano

DOI:
10.1016/j.ifset.2019.102231

Document Version
Peer reviewed version

Citation for published version (Harvard):
Jabarkhyl, S, Barigou, M, Zhu, S, Rayment, P, Lloyd, DM & Rossetti, D 2020, 'Foams generated from viscous non-Newtonian shear-thinning liquids in a continuous multi rotor-stator device', *Innovative Food Science and Emerging Technologies*, vol. 59, 102231. https://doi.org/10.1016/j.ifset.2019.102231

Foams generated from viscous non-Newtonian shear-thinning liquids in a continuous multi rotor-stator device

Saifullah Jabarkhyl[1], Mostafa Barigou[1]*

Shiping Zhu[2], Pip Rayment[2], David M. Lloyd[2], Damiano Rossetti[2]

[1]School of Chemical Engineering, University of Birmingham, Edgbaston, Birmingham B15 2TT, UK
[2]Unilever R&D Refreshment Discovery, Colworth Science Park, Sharnbrook, MK44 1LQ, UK

Abstract

Whilst aeration is ubiquitous in the food industry, little work has been done on foams generated from viscous non-Newtonian liquids. We study the production of foams from viscous shear-thinning liquids containing a non-ionic food grade surfactant (PGE 55), Xanthan gum and caster sugar, using a continuous pilot-scale device having twelve rotor-stator pairs. The effects of process parameters (rotor speed, gas-liquid volumetric flowrate ratio (G/L)) and liquid composition (surfactant concentration, Xanthan gum concentration) on foam gas volume fraction and bubble size distribution are elucidated. X-ray micro-Computed Tomography is employed to characterise the 3D microstructure of the foams. Rotor speed and G/L ratio are the dominant factors in determining the gas volume fraction and bubble size distribution. The foams produced exhibit a rich fine texture with high static stability. For a given energy input, a higher G/L ratio results in a higher gas fraction and a smaller bubble size.

Keywords: Continuous foaming; non-Newtonian liquid; X-ray micro-CT; Rheology; Bubble size distribution.

***Corresponding author: m.barigou@bham.ac.uk**

1. Introduction

Over the last 30 years, aerated food products have become increasingly popular since the inclusion of air bubbles gives rise to a variety of microstructures which exhibit better textural and sensorial properties (Campbell & Mougeot, 1999; Guo et al., 2017; Indrawati & Narsimhan, 2008). Depending on the gas volume fraction (ϕ), aerated food products can be classified as wet foam (~ $0.50>\phi<0.95$) or dry foam (~ $\phi>0.95$). A foam consists of a continuous liquid phase in the form of a network of thin lamellae and a dispersed gas phase in the form of bubbles ranging from microns to millimetres in size (Bikerman, 1973; Walstra, 1989). Foams are thermodynamically unstable structured fluids (Curschellas et al., 2012a; Corina Curschellas et al., 2012b; Germain & Aguilera, 2014). They are subject to three distinct destabilisation mechanisms: liquid drainage, bubble coalescence and disproportionation (Cox, Aldred, & Russell, 2009; Kroezen & Wassink, 1987).

In the production of aerated products such as whipped cream, ice cream or mousse, it is important to achieve a good degree of control of the air volume fraction and bubble size distribution since the stability and the organoleptic properties of the product (creaminess, texture, mouthfeel) are strongly dependent on these critical parameters. For example, small bubbles and uniform bubble size distribution impart excellent foam stability and creaminess (Müller-Fischer, Suppiger, & Windhab, 2007b; Müller-Fischer & Windhab, 2005). Many techniques have been proposed for measuring bubble size distribution including conductivity probes, optical fibre technique, light microscopy, freezing and visualising foam cross-sections, X-ray micro-computed tomography (X-ray micro-CT), ultrasonic reflectance spectroscopy and confocal scanning laser microscopy (Jang, Nikolov, Wasan, Chen, & Campbell, 2005; Kulmyrzaev, Cancelliere, & McClements, 2000; Lim & Barigou, 2004). Each of these methods has its own advantages and drawbacks. For example, light microscopy which is commonly used is usually intrusive as it often requires sampling the foam and sometimes diluting the sample especially when the bubble size is small and the bubble density is high. Other techniques suffer from similar limitations which involve significant tampering with the foam samples. By contrast, however, X-ray micro-CT is a non-destructive and non-intrusive technique and can be utilised to image stable foams to reveal their full 3D microstructure with a high degree of accuracy (Lim & Barigou, 2004).

Food foams are generated using a number of different techniques including mechanical whipping, membrane foaming, gas sparging (Pugh, 2016). At pilot and industrial scales, mechanical whipping devices are preferred as they are more amenable to continuous large-scale production and better process control. In this respect, continuous rotor-stator devices are popular especially when processing viscous and non-Newtonian liquids (Hanselmann & Windhab, 1998; Kroezen, Groot Wassink, & Bertlein, 1988; Kroezen & Wassink, 1987; Mary et al., 2013; Mezdour, Séguineau de Préval, Granda, Cuvelier, & Ducept, 2017; Müller-Fischer et al., 2007b; Narchi, Vial, Labbafi, &

Djelveh, 2011; Nicorescu et al., 2010). The first study using a continuous rotor-stator device was by Krozen and Wassink (1988). Smaller bubbles were obtained at higher rotational speeds and lower air volume fractions. In addition, air inclusion was found to be good in the turbulent flow regime, poor in transitional flow and moderate in laminar flow. A number of studies then followed which studied the effects of liquid mix properties (density, viscosity and surface tension) and processing parameters (rotor speed, air volume fraction, power input, residence time, static pressure and temperature in the mixing-head chamber). For example, using a single non-Newtonian fluid and a fixed twelve rotor-stator geometry operating at a single speed, Muller-Fischer and Windhab (2005) found that bubble size increased as the gas-liquid ratio inside the mixing-head chamber was increased (G/L = 0.5–3.5) covering laminar to transitional flow, and this was attributed to bubble coalescence. Nicorescu et al. (2010), on the other hand, using a fixed seven rotor-stator geometry, a fixed non-Newtonian fluid and a single G/L ratio of 2.0, investigated the effects of rotor speed and residence time on aeration efficiency and bubble size. Rotor speed was found to be the main processing parameter affecting bubble size, but no reference was made to the flow regime and how it influences bubble size and aeration efficiency. Narchi et al. (2011) also investigated the effects of rotor speed on bubble size for a fixed Newtonian and a fixed non-Newtonian medium under laminar conditions. For both fluid systems, bubble size was found to decrease with rotor speed. For the Newtonian fluid, bubble size also decreased as a function of G/L ratio but no explanation was given. This effect was not investigated for the non-Newtonian system.

No systematic studies have hitherto been reported on the combined effects of liquid composition (surfactant concentration, thickener concentration) and processing parameters (rotor speed, G/L ratio) for non-Newtonian media which are most relevant to the production of food foams. Furthermore, the vast majority of the literature on continuous foaming has considered model food foams stabilized by proteins, with non-ionic surfactants receiving much less attention. Apart from their different absorption kinetics, the mechanisms of bubble stabilization by the latter surface active agents are also different. In this paper, we present the first extensive study of wet foams generated from viscous non-Newtonian shear-thinning liquids using a continuous multi rotor-stator device and a non-ionic surfactant. A range of experimental conditions are investigated to determine the effects of liquid formulation and processing conditions on foam bubble size distribution, gas volume fraction and static stability. Foaming is carried out under atmospheric conditions to avoid foam expansion which can bring about drastic changes in foam microstructure which is uncontrollable and undesirable (Müller-Fischer et al., 2007b). We use an advanced X-ray micro-CT technique to non-invasively visualise and analyse the 3D microstructure of the foams.

2. Materials and methods

2.1 Model fluids preparation and characterisation

The model fluids employed in the experiments consisted of a mixture of polyglycerol fatty acid ester (PGE 55, DuPont, Denmark), Xanthan gum (XG, supplied by Unilever), caster sugar (British sugar PLC, obtained from local supermarket) and sodium azide (ReagentPlus, ≥99.5%, Sigma Aldrich), used without prior purification. A Silverson high-shear mixer (Model L4RT, Silverson, UK) was used to mix the ingredients in distilled water held at 80°C using a water bath, to ensure that the Krafft temperature (58°C) of PGE 55 was exceeded (Curschellas et al., 2012a; Duerr-Auster, Eisele, Wepf, Gunde, & Windhab, 2008). First, polyglycerol fatty acid ester (PGE 55) was added under agitation (6000-7000 rpm) and mixed thoroughly for at least 5 minutes prior to adding sugar and XG. Stirring was continued for another 5 min until all XG was completely dissolved. Sodium azide (0.025 wt%) was added to prevent microbial growth. The model fluids were then stored at room temperature to degass and mature (hydration of XG) for at least 24 hours, to enable their rheology to fully stabilise. In order to check that the high-shear processing used did not affect the rheology of the fluids, we also prepared smaller volumes of such liquids using gentle mixing provided by a magnetic stirrer. There was no significant difference between the liquids obtained.

The equilibrium surface tension of the fluids was measured at 25°C using a Wilhelmy plate method (Sigma 701 Force Tensiometer). Dynamic surface tension measurements were obtained using a pendant drop method (PAT1P Tensiometer, Sinterface, Germany). Prior to any measurement, solutions were centrifuged for 4 minutes at a rotational speed of 2800 rpm to remove entrapped air bubbles. Each measurement was repeated at least three times and an average taken (SD = 1.5 mN m^{-1}).

Table 1 summarises the composition of the model fluids and their physical properties; the density of all fluids was equal to 1080 kg m^{-3}. The presence of caster sugar and XG, had negligible effects on the surface tension as the surface activity of PGE 55 is much greater than both caster sugar and XG. For all model fluids tested, surface tension was shown to evolve with respect to time, with a rapid initial reduction followed on by a gradual decline tending towards an equilibrium value. Equilibrium values of surface tension are given in Table 1. As shown and expected, surface tension kinetics was found to be a function of PGE 55 and XG concentration.

A controlled stress/strain rheometer (Discovery HR-2, Hybrid Rheometer, TA, USA) equipped with a 40 mm parallel plates geometry was used to characterise the rheology of the model fluids. No slip was detected and measurements conducted using different plate gaps (and alternatively a cone-and-plate geometry) yielded the same results. Complete flow curves were obtained at controlled strain rate by varying the shear rate in the range of 0.001–8000 s^{-1}, and were well fitted by the Cross rheological model (coefficient of determination, $R^2 \sim 0.999$). The cross model incorporates both the

upper and limiting viscosities, η_o and η_∞, corresponding, respectively, to the upper and lower Newtonian regions, and is given by:

$$\eta = \eta_\infty + \frac{\eta_0 - \eta_\infty}{1+(c\dot{\gamma})^m} \quad (1)$$

where η is the apparent viscosity, $\dot{\gamma}$ is the shear rate, and c and m are the Cross time constant and rate constant, respectively. This model can be reduced to the power law model in the region where $\eta << \eta_o$ and $\eta >> \eta_\infty$, which will be useful for the definition of a modified Weber number, as discussed further below.

2.2 Foam generation

A pilot-scale continuous rotor-stator (Megatron FM 12- 50/2 HR), shown in Fig. 1, was used to aerate the model fluids and continuously generate foam. The device consists of 12 rotor-stator pairs in series where the rotor and stator have diameters of 50 and 43 mm each. Every rotor and stator has 13 pins (4.7 x 4.6 x 2.5 mm) with square ends and the gap between the rotor and stator is 1.0 mm. The geometrical dimensions of the rotor-stator pairs are provided in Table 2.

A progressive cavity pump is utilised to continuously pump the liquid at a controlled flowrate to the mixing-head chamber which has a free volume of approximately 85 mL. Simultaneously, a controlled amount of air is also introduced into the feed line from a gas cylinder, which combines with the liquid upon entering the mixing-head chamber. Foam was generated at atmospheric pressure using rotor speeds in the range 500-1750 rpm. A Julabo F-25 cooler (JULABO GmbH, Germany) was used to dissipate the heat generated during operation and control the mixing-head temperature, so that the exit foam temperature was maintained approximately equal to the liquid feed temperature at 20 ± 3°C, which kept the effects on fluid rheology and surfactant kinetics minimal.

Experiments were conducted to generate foams with varying microstructure by using combinations of liquid flowrate values within the range 3.46 – 6.67 $Lh^{-1}$and air flowrate values within the range 5.0 – 10.1 Lhr^{-1}. These experiments showed a high degree of reproducibility in terms of foam gas volume fraction and mean bubble size, i.e. within 5% at the lowest rotor speed and within 1% at the highest speed.

2.3 Foam characterisation

2.3.1 *Air volume fraction*

The air volume fraction in the foam is theoretically defined as:

$$\emptyset_{th} = \frac{Q_G}{Q_G + G_L} \quad (2)$$

where Q_G and Q_L are, respectively, the air and liquid volumetric flowrate. This was experimentally measured by collecting foam samples at the exit of the rotor-stator device and determining the average mass of base liquid and foam that fill the same volume. The experimentally measured ϕ_e value cannot be greater than the theoretical value ($\emptyset_{th}$). An efficient foaming process will aim to maximise ϕ_e.

2.3.2 *Bubble size distribution*

Two techniques were utilised to obtain the foam bubble size distribution. The first technique is a well-established method which uses a light microscope (ZEISS, Axiovert 200M) and a digital camera. Foam samples were diluted using the base liquid and then carefully transferred to a viewing chamber according to the protocol described by Gaillard et al. (2017). A minimum of 500 bubbles were measured in each sample to avoid statistical bias, using ImageJ software (https://imagej.nih.gov/ij/index.html). The second method used a desktop X-ray micro-CT (Skyscan 1172, Bruker, Belgium) to scan and visualise, non-invasively, the full 3D microstructure of the foam samples (3.8 µm resolution). A 2-5 mL foam sample was placed inside a drinking straw and sealed prior to scanning (Barigou & Douaire, 2013; Lim & Barigou, 2004). From the bubble size distribution, the Sauter mean bubble diameter was obtained:

$$D_{32} = \frac{\sum n_i d_i^3}{\sum n_i d_i^2} \tag{3}$$

where n is the number of bubbles of diameter d in class size i.

2.3.3 *Foam stability*

Foam stability is determined by liquid drainage, bubble coalescence and Ostwald ripening. Foam drainage was measured over a period of many weeks by monitoring a 50 mL foam sample collected at the outlet of the continuous rotor-stator and stored at a constant temperature of 25°C. Thus, transients of drained liquid were obtained for all experimental conditions investigated. Foam collapse was measured by monitoring the height of standing foams. Foam coarsening which is a consequence of bubble coalescence and Ostwald ripening was investigated using X-ray micro-CT, by scanning foam samples also stored at constant temperature (25°C) on a weekly basis over a period of several weeks.

2.3.4 *Foam rheology*

Foam rheometry was conducted at 25°C using the stress/strain controlled rheometer and parallel-plate geometry described above. In this case, minor slip was observed but this was eliminated by using roughened plates (58 µm equivalent grit size). The parallel-plate gap was fixed at 2 mm which is approximately an order of magnitude larger than the largest bubble size. Complete flow curves were obtained at controlled strain rate by varying the shear rate in the range of 0.0001−1000 s^{-1}, and were well fitted by the Cross model (coefficient of determination, $R^2 \sim 0.999$) defined in Eq. (1).

2.4 Theory

2.4.1 Foam hydrodynamics inside mixing-head chamber

The Hydrodynamics inside the mixing-head chamber play a crucial role in the production of homogenous foams. The pertinent parameters are the Power number and the Reynolds number. The Power number is the dimensionless form of the power input (*P*):

$$P_o = P/\rho_f N^3 D^5 \quad (4)$$

where *N* is the rotor speed and ρ_f is the density of the gas-liquid dispersion. The Power number is in turn dependent on the value of Reynolds number (*Re*) defined as follows:

$$P_o = f(Re) \quad (5)$$

where *Re* is given by:

$$Re = \rho_f N D^2/\eta(\dot{\gamma}) \quad (6)$$

where $\eta(\dot{\gamma})$ is the apparent foam viscosity at shear rate $\dot{\gamma}$.

Krozen and Wassink (1988) were the first to derive via an extensive study the empirical relationship $P_o = f(Re)$ for a continuous rotor-stator device, by experimenting with different geometries and a wide range of water-glycerol mixtures. Such a relationship was based on a generalised Power number:

$$P_o^* = Pz/\rho_F D^4 N^3 hLq \quad (7)$$

and a generalised Reynolds number :

$$Re^* = \rho_F NDs/(f \times \eta(\dot{\gamma})) \quad (8)$$

both of which are independent of rotor-stator device geometry. The correlation factor *f* in Eq. (8) is defined as:

$$f = 71o/q + 553s/\sqrt{Dq} \quad (9)$$

and the geometrical dimensions h, L, q, o and s are defined in Table 2. In the laminar flow regime ($Re^* < 0.01$), the Power number was found to be inversely proportional to the Reynolds number, whereas in the turbulent regime ($Re^* > 0.1$), P_o^* was found to be constant (equal to 17).

2.4.2 Energy dissipation inside mixing-head chamber

The energy consumption in our foaming experiments was estimated using the above empirical relationship $P_o = f(Re)$ developed by Krozen and Wassink (1988). This initially involved the identification of the flow regime using the definition of *Re** (Eq. (8)) and *f* (Eq. (9)), the dimensions of the rotor-stator geometry (Table 2) and the function $\mu(\dot{\gamma})$. For all experimental conditions investigated, *Re** was found to be in the range of 0.02–5.7, i.e. corresponding in the vast majority to turbulent flow where, as indicated above, P_o^* is constant and equal to 17.

The net mechanical power input per unit volume (P_v) is defined as:

$$P_v = \frac{P}{V} \tag{10}$$

where *V* is the volume of the mixing-head chamber (85 mL). The shear rate ($\dot{\gamma}$) inside the mixing-head chamber is the maximum shear rate at the tip of the rotor (Müller-Fischer, Bleuler, & Windhab, 2007a):

$$\dot{\gamma} = \frac{\pi DN}{s} \tag{11}$$

The viscosity function of the foam $\eta(\dot{\gamma})$ is obtained by determining the rheological flow curve of foam samples taken at the outlet of the rotor-stator device using the rheometer described above. Finally, the net volumetric energy input (E_V) can be determined, thus:

$$E_V = \tau P_v \tag{12}$$

where τ is the average residence time of both the gas and liquid in the mixing-head chamber, given by:

$$\tau = \frac{V}{V_{foam}} = \frac{V}{Q_L + Q_G} \tag{13}$$

where V_{foam} is the volumetric flowrate of foam and Q_L and Q_G are the liquid and air volumetric flowrate, respectively.

3 Results and discussion

3.1 Aeration efficiency

Aeration efficiency is an important feature of the foam generation process which indicates the ability to incorporate all of the available gas into the foaming liquid to make a homogeneous foam. Thus, optimum aeration is achieved when the theoretical and experimental values of volume gas fraction (ϕ) are equal (Eq. (2)). We studied the effects on the incorporated gas volume fraction of the processing parameters (rotor speed, air and liquid volumetric flowrates) and the physical properties of the liquid (dynamic surface tension, liquid viscosity). In the first set of experiments, the liquid flowrate was set to 5 L hr^{-1} and the air flowrate was varied between 5, 7.5 and 10.0 L hr^{-1} to achieve foams with $\emptyset_{th}$ values in the range of 0.50-0.67. When the G/L ratio was set to 1.0, all model fluids were able to achieve maximum aeration, i.e. $\emptyset_e = \emptyset_{th}$, over the range of rotational speed 500-1750 rpm, independent of the residence time (τ) and the composition of the liquid used, as shown in Table 3.

However, when the G/L ratio was increased to 1.5, a 'blow-by' phenomenon was observed for MF1 at rotational speeds of 500 and 750 rpm and this was also independent of τ. The term 'blow-by' was initially coined by Kroezen and Wassink (1988) who observed a large pocket of undispersed gas (slug flow regime) at the outlet of the continuous rotor-stator, which is undesirable. The moderate concentration of PGE 55 (0.2 wt%) seems to limit the incorporation of air in liquid MF1 at these particular rotational speeds. This phenomenon may be attributed to bubble coalescence inside the mixing-head chamber due to insufficient surfactant, as previously observed in turbulent emulsification (Tcholakova et al., 2011). As G/L was increased, 'blow-by' occurred at higher and higher rotational speeds and no homogeneous foam could be produced at any speed within the range studied when G/L $\geq$ 2.5. Fluids MF2 and MF3, with a higher PGE 55 content (0.5 wt% and 1 wt%, respectively), were in fact able to achieve maximum air volume fraction at all rotational speeds investigated when G/L = 1.5. 'Blow-by' was observed, however, for both fluids regardless of residence time when G/L = 2.0 at rotational speeds of 500 and 750 rpm, and at G/L = 2.5 it occurred at all rotational speeds. Thus, a doubling in PGE 55 concentration between MF2 and MF3 had no influence on the onset of 'blow-by'. Fluids M4 and M5 have the same surfactant concentration as fluid MF2 but a lower Xanthan gum concentration (Table 1); they exhibit 'blow-by' under the same conditions as MF2 but their foam stability, bubble size distribution and rheological properties are significantly different. These results seem to suggest that beyond a certain concentration, the aeration process is no longer determined by surfactant content or the hydrodynamics of the process.

3.2 Comparison between light microscopy and X-ray micro-CT

Typical foam images produced from light microscopy and X-ray micro-Computed Tomography, described above, are shown in Fig. 2. The corresponding Sauter mean bubble diameter (D_{32}) data are plotted in Fig. 3 for G/L = 1 and 1.5. As shown, there are significant discrepancies between the two sets of results. Light microscopy is a 2D technique which suffers from a number of shortcomings

including: (i) out-of-focus bubbles have to be manually detected and removed; any out-of-focus bubbles not filtered out may introduce errors; (ii) bubbles larger than the gap of the viewing cell are distorted, thus, giving rise to errors; and (iii) the size of bubble sample analysed (~ 500-1000) is limited by the slow and tedious semi-automatic image processing. In comparison, X-ray micro-CT is a non-invasive technique which yields the full 3D structure of the foam which can then be sliced and examined along any plane. The number of 3D bubbles analysed in X-ray micro-CT is much greater (~ 5000-15000) and the analysis is fully automated. In conclusion, the 3D X-ray micro-CT technique is a more accurate and reliable technique and was adopted for the characterisation of the foams in this study. More details on the advantages of X-ray micro-CT can be found in Barigou and Douaire (2013).

3.3 Effects of processing parameters and physical properties of foaming solution on bubble size

3.3.1 Effects of G/L ratio and residence time

The effects of varying the rotor speed on the Sauter mean bubble diameter of the foam are shown in Fig. 4 for fluids MF1, MF2 and MF3 at different G/L ratios. Irrespective of the model fluid and G/L ratio, increasing *N* leads to a sharp reduction in bubble size as widely reported in the literature where similar rotor-stator devices were used (Balerin, Aymard, Ducept, Vaslin, & Cuvelier, 2007; Mary et al., 2013; Müller-Fischer et al., 2007b; Narchi et al., 2011; Nicorescu et al., 2010; Seguineau De Preval, Fabrice, Gérard, & Samir, 2014a; Seguineau De Preval, Fabrice, Gilles, Gérard, & Samir, 2014b). This reduction is mainly due to the increased shear, elongation and inertia forces acting inside the mixing-head chamber which break down larger air bubbles into smaller bubbles (Müller-Fischer et al., 2007b). In addition, increasing *N* leads to a narrower and more uniform bubble size distribution, as shown in Fig. 4.

For a given fluid and a given rotational speed, increasing the G/L ratio results in a considerable reduction in bubble size (D_{32}), as shown in Fig. 4. This result is counter-intuitive since an increase in G/L reduces the foam residence time (Fig. 4) in the mixing-head chamber, thus, leading to less shearing of the gas-liquid dispersion. Over the range of rotor speeds studied (500-1750 rpm), *N* does not affect the residence time. The residence time inside the mixing-head chamber which has a fixed volume and a fixed number of rotor-stator pairs (12) can be varied only by changing the G/L ratio (Eq. 13). As shown by the data in Fig. 5 and Table 3, the same value of τ corresponds to different G/L ratios but the same G/L ratio may lead to different values of τ and different dispersion viscosities. Hence, the effects of τ on bubble size are complicated and hard to interpret (Balerin et al., 2007; Mary et al., 2013).

The reduction in bubble size caused by increasing the G/L ratio, however, can be explained by the significant rise in the apparent viscosity of the dispersion inside the mixing-head chamber when the

G/L ratio is increased, as shown in Fig. 5. The shear rate inside the mixing-head chamber was estimated using Eq. (11) and used to predict the apparent viscosity of the model fluids and gas-liquid dispersion using Eq. (1). An increase in apparent viscosity enhances the shear stresses acting on the bubbles leading to a reduction in bubble size (Indrawati & Narsimhan, 2008). As shown in Fig. 6, foam generated from MF2 at G/L = 1.5 exhibits a much more uniform bubble size distribution compared to foam generated at G/L = 1.0. Muller-Fischer et al. (2007a), using a dynamically enhanced membrane foaming technique, found that an increase in air volume fraction led to a reduction in bubble size which they attributed to an increase in dispersion viscosity. Similarly, increasing the disperse phase volume fraction in emulsions has also been reported to lead to a reduction in droplet size and polydispersity in the turbulent flow regime (Tcholakova et al., 2011; Vankova et al., 2007).

3.3.2 Effects of surfactant concentration

The effects of surfactant concentration on foam bubble size are depicted in Fig. 7. Fluids MF1, MF2 and MF3 are identical except for their different surfactant content. For G/L = 1.0, a higher concentration of PGE 55 from MF1 to MF2, to MF3 does not result in significant difference in mean bubble size. At higher G/L values, e.g. G/L = 1.5, a higher surfactant concentration initially leads to a much smaller bubble size (MF1 and MF2) but no further effect is observed beyond a certain concentration; MF2 and MF3 have concentrations of 0.5 wt% and 1.0 wt%, respectively, but exhibit the same mean bubble size at all rotational speeds. These effects are visualised in Fig. 8 showing sample X-ray micro-CT images of the different foam microstructures. This bubble size behaviour has previously been reported for Newtonian fluids (Seguineau De Preval et al., 2014a; Seguineau De Preval et al., 2014b). The same trend was followed by the volume gas fraction, as discussed above.

As shown in Fig. 9, changing the surfactant concentration alters the surface tension kinetics especially at short time scales similar to the processing times (<100s). At higher PGE 55 concentrations up to ~ 0.5 wt%, the higher availability of surfactant molecules and their ability to diffuse faster to the air-water interfaces leads to the formation of smaller bubbles. Thereafter, the solution is saturated with surfactant and more PGE 55 produces no effect on surface tension kinetics and, hence, bubble size.

3.3.3 Effects of Xanthan gum concentration

A higher XG concentration leads to a reduction in foam bubble size at all rotor speeds, but beyond a certain value the effect becomes negligible, as visualised in the images of Fig. 10 and represented in the mean bubble size plots in Fig. 11a. This has also been previously observed for foams generated from Newtonian fluids (Mary et al., 2013; Seguineau De Preval et al., 2014a; Seguineau De Preval et al., 2014b) and non-Newtonian shear-thinning fluids (Balerin et al., 2007; Hanselmann & Windhab, 1998; Indrawati & Narsimhan, 2008).

There are two competing factors which are affected by changing the XG concentration, namely the apparent viscosity and the surface tension kinetics, as shown in Figs. 11b and 11c, respectively. As discussed above, a higher dispersion viscosity arising from a higher XG content can, up to a point, lead to a finer foam texture in the mixing-head chamber due to higher shear stresses which produce smaller bubbles and slower drainage which prevents bubble coalescence (Indrawati & Narsimhan, 2008). At the same time, the slower surface tension kinetics arising from a higher XG content, up to a point, lead to the formation of larger bubbles since the surfactant diffuses more slowly to air-water interfaces. The results obtained here indicate that the viscosity effects are predominant.

3.4 Theoretical analysis

3.4.1 Data reduction for interpretation of bubble size

The above results can be generalised by interpreting the data in terms of the Weber number, a ratio of shear forces to capillary pressure acting on the bubble. Typical apparent viscosity curves of the model fluids used and the foams produced are represented in Fig. 12. As pointed out above, the Cross model (Eq. 1) used to represent the apparent viscosity curves of the foam can be reduced in the central shear-thinning region ($\eta_\infty << \eta << \eta_o$) which covers the entire experimental conditions of this study to the much simpler two-parameter power law model:

$$\eta = k\dot{\gamma}^{n-1} \tag{14}$$

where k is the consistency index, n is the flow behaviour index. This facilitates the definition of a modified critical Weber number, thus:

$$We = \frac{k(ND)^n}{\sigma_e s^{n-1}} \tag{15}$$

where σ_e is the equilibrium surface tension value reached after at least one hour (Fig. 9).

Different authors have adopted different definitions of *We* for foam taking into consideration the geometrical dimensions of the foam generating device, the hydrodynamics and liquid composition. A constant value of 0.24–0.60 is commonly reported for the critical Weber number at which bubbles rupture (Balerin et al., 2007; Kroezen et al., 1988; Thakur, Vial, & Djelveh, 2005). Thakur et al. (2003), however, using time and shear rate dependent non-Newtonian liquids in a mechanical agitator device, found that *We* increased as a function of rotor speed. Similarly, using a continuous rotor-stator device and Newtonian media, Balerin et al. (2007) reported the same result; the increase in this case was attributed to a rise in local heat dissipation at higher rotor speeds.

The variations of foam mean bubble size are plotted in Fig. 13 as a function of *We* for the various experimental conditions investigated including all G/L ratios. The data follow the same general trend showing D_{32} decreasing with *We* (Fig. 13a). The best line fitted through the data shows, however, a significant amount of scatter (± 20 %). When the data are plotted for G/L ≥ 1.5 only, in Fig. 13b, the data collapse on a single line with much little scatter (± 10 %). This can be explained by the fact that data for G/L = 1.0 correspond to an inertial turbulent flow regime where the eddy scale is smaller than the bubble size and, hence, do not fit in with data for G/L>1.5 which correspond to a viscous turbulent flow regime where the eddies are larger than the bubble size. It is interesting to note that if the results for MF2, M4 and MF5 at G/L = 1.5, with the same surfactant concentration but a lower XG concentration, are plotted separately (Fig. 13c), the data collapse on a single line with little scatter (± 5 %). Indrawati and Narsimhan (2008) reported similar observations using a mechanically agitated vessel to generate their foam, but this result is hard to explain.

Overall, these findings show that a general (approximately) unified curve can be obtained with such complex systems which, when produced for one fluid formulation, could be used to interpret data of foams in different non-Newtonian media. This result should simplify the prediction of foam texture.

3.4.2 Effects of energy input on foam microstructure

The energy input during the production of foam using a continuous rotor-stator is an important parameter for process design and optimisation. For a given fluid formulation and a fixed rotor-stator geometry, energy dissipation inside the mixing-head chamber can be controlled by either changing the rotational speed or the G/L ratio. The rotor speed affects the shear stresses acting within the mixing-head chamber, whereas G/L ratio controls the residence time (τ), and both parameters impact the bubble size distribution and, hence, the microstructure of the foam. Thus, the effects of *N* and G/L on gas volume fraction and bubble size distribution were investigated.

Typical variations of the net volumetric energy input (E_v) with *N* and G/L ratio are depicted in Fig. 14 for foams produced from fluid MF2. As expected, for a given G/L ratio, E_v increases exponentially as a function of *N*. As G/L increases (and hence τ reduces), E_v diminishes considerably. Hence, generating foams with a higher gas fraction requires less energy input. Bubble size, on the other hand, follows an exponential decay as more energy is dissipated inside the mixing-head chamber (Fig. 15). As previously pointed out, increasing the G/L ratio increases the apparent viscosity of the dispersion which enhances the shear forces inside the mixing-head chamber to break down larger air bubbles into smaller bubbles. Thus, for a given amount of energy dissipation, a higher G/L ratio leads to a smaller bubble size. Hence, for a given E_v, a higher G/L ratio results in a higher gas fraction and a smaller bubble size, i.e. a richer foam with a finer texture.

3.5 Foam stability

Static foam stability is governed by the combined effects of foam drainage, collapse and coarsening. Foam drainage and collapse were measured over a long period of time (~ 1300 hr) by monitoring foam samples collected at the outlet of the rotor-stator device and stored in a controlled environment. Foam drainage and collapse profiles are shown in Fig. 16 for MF2 at G/L = 1.0. In general, both drainage and collapse are very slow indicating that the foams are very stable. Foams produced at higher rotor speeds exhibit slower drainage. As discussed above, increasing *N* leads to a significant reduction in bubble size and a narrower bubble size distribution. This results in an increase in foam stability due to the higher liquid flow resistance through the thinner lamellae and Plateau borders network (Nicorescu et al., 2010). The use of XG imparts non-Newtonian characteristics to the continuous phase including a high zero-shear Newtonian viscosity (Fig. 12; sometimes confused in the literature with the existence of a yield stress) which counters gravitational drainage and gives high stability to the foam. In addition, PGE 55 can form multilamellar vesicles in the liquid which can significantly hinder liquid drainage by obstructing the Plateau borders (Curschellas et al., 2012a; C. Curschellas et al., 2012b; Curschellas et al., 2013). Therefore, higher XG or PGE 55 concentrations improve foam stability. Furthermore, increasing the G/L ratio, as discussed above, increases the air volume fraction which reduces the liquid contained within the foam (Plateau borders and lamellae) and the foam stability is enhanced (data not shown). For example, at G/L = 1.5, the rate of drainage is slowed down by an order of magnitude and no foam collapse is observed within 1300 hr.

Foam coarsening was assessed over several weeks via X-ray micro-CT using similar foam samples, as shown in Fig. 17. The use of the non-ionic surfactant PGE 55 provided excellent resistance to bubble coalescence as its molecules/vesicles irreversibly adsorb at gas-liquid interfaces (Curschellas et al., 2013). Foam coarsening was found to be generally slow. Foams generated at higher rotor speeds had finer bubbles (i.e. faster air diffusion and disproportionation) and thinner foam lamellae (i.e. more coalescence) which led to faster foam coarsening. Whilst high G/L ratios lead to slower drainage and collapse, they undergo faster coarsening (data not shown) due to their thinner lamellae separating the neighbouring bubbles. It is also known that PGE 55 can irreversibly adsorb to an air-water interface and hence provide steric stabilisation against bubble coalescence (Duerr-Auster, Gunde, Mäder, & Windhab, 2009).

4. Conclusions

This study focused on the production of foams from viscous shear-thinning liquids using a pilot-scale continuous multi rotor-stator device operating at atmospheric pressure. The effects of process parameters (rotor speed, G/L ratio) and liquid formulation (surfactant concentration, Xanthan gum concentration) on foam gas volume fraction and bubble size distribution were studied. Rotor speed and G/L ratio were the dominant factors in determining the gas volume fraction and bubble size

distribution. Higher rotor speed which implies higher energy input, led to finer texture foams. Increasing the G/L ratio led to a reduction in average residence time but, counter-intuitively, reduced foam bubble size and polydispersity. This was attributed to an increase in the apparent viscosity of the dispersion which in turn enhances the shear forces inside the mixing-head chamber to break down larger air bubbles into smaller bubbles. Hence, for a given energy input, a higher G/L ratio results in a higher gas fraction and a smaller bubble size, i.e. a richer foam with a finer texture. The foams produced exhibited a high static stability over long periods of time. Higher rotor speeds and G/L ratios resulted in slower drainage and collapse , but foam coarsening was faster.

Acknowledgements

Saifullah Jabarkhyl's PhD research was funded by EPSRC and Unilever Colworth (UK).

Notation

D	rotor diameter (m)
d	bubble diameter (m)
D_{32}	sauter mean diameter (m)
E_V	specific energy per m^3 of foam processed (J m^{-3})
f	correlation factor (-)
F	*frequency (%)*
h	number of rotor-stator pairs (-)
h_f	foam collapse (m)
I	number of pins on rotor (-)
k	consistency index (Pa $s^{n'}$)
L	diameter of annulus mixing space (m)
MF1	model fluid 1 (-)
MF2	model fluid 2 (-)
MF3	model fluid 3 (-)
MF4	model fluid 4 (-)
MF5	model fluid 5 (-)
N	rotational speed (s^{-1})
n	flow behaviour index (-)
n_i	number of bubble with diameter i (-)
o	width of rotor pin (m)
$P_{v,diss}$	net volumetric power input (J s^{-1} m^{-3})
P_0	Power number (-)
P^*_0	generalised Power number (-)
PGE 55	polyglycerol ester of fatty acid (-)

q	height of rotor/stator pin (m)
Q_L	liquid volumetric flowrate ($m^3\ s^{-1}$)
Q_G	gas volumetric flowrate ($m^3\ s^{-1}$)
Re	Reynolds number (-)
Re^*	generalised Reynolds number (-)
s	distance between rotor-stator (m)
V	volume of mixing-head chamber (m^3)
v_L	liquid drained (m^3)
We	Weber number (-)
XG	Xanthan gum (-)
X-ray micro-CT	X-ray micro-Computed Tomography (-)
$z = \frac{\pi D}{I}$	distance between rotor pins (m)

Greek symbols

τ	average residence time (s)
η	apparent viscosity (Pa.s)
ρ	density ($kg\ m^{-3}$)
σ	surface tension ($N\ m^{-1}$)
Ø	air volume fraction (-)
$\dot{\gamma}$	shear rate (s^{-1})

References

Balerin, C., Aymard, P., Ducept, F., Vaslin, S., & Cuvelier, G. (2007). Effect of formulation and processing factors on the properties of liquid food foams. *Journal of Food Engineering, 78*(3), 802-809. doi:http://doi.org/10.1016/j.jfoodeng.2005.11.021

Barigou, M., & Douaire, M. (2013). 9 - X-ray micro-computed tomography for resolving food microstructures. In V. J. Morris & K. Groves (Eds.), *Food Microstructures* (pp. 246-272): Woodhead Publishing.

Bikerman, J. J. (1973). *Foams*. New York: Springer-Verlag.

Campbell, G. M., & Mougeot, E. (1999). Creation and characterisation of aerated food products. *Trends in Food Science & Technology, 10*(9), 283-296. doi:http://doi.org/10.1016/S0924-2244(00)00008-X

Cox, A. R., Aldred, D. L., & Russell, A. B. (2009). Exceptional stability of food foams using class II hydrophobin HFBII. *Food Hydrocolloids, 23*(2), 366-376. doi:https://doi.org/10.1016/j.foodhyd.2008.03.001

Curschellas, C., Gunes, D. Z., Deyber, H., Watzke, B., Windhab, E., & Limbach, H. J. (2012a). Interfacial aspects of the stability of polyglycerol ester covered bubbles against coalescence. *Soft Matter, 8*(46), 11620-11631. doi:10.1039/C2SM26446C

Curschellas, C., Keller, R., Berger, R., Rietzler, U., Fell, D., Butt, H.-J., & Limbach, H. J. (2012b). Scanning force microscopy as a tool to investigate the properties of polyglycerol ester foams. *Journal of Colloid and Interface Science, 374*(1), 164-175. doi:https://doi.org/10.1016/j.jcis.2012.01.031

Curschellas, C., Kohlbrecher, J., Geue, T., Fischer, P., Schmitt, B., Rouvet, M., . . . Limbach, H. J. (2013). Foams Stabilized by Multilamellar Polyglycerol Ester Self-Assemblies. *Langmuir, 29*(1), 38-49. doi:10.1021/la3029116

Duerr-Auster, N., Eisele, T., Wepf, R., Gunde, R., & Windhab, E. J. (2008). Influence of pH on colloidal properties and surface activity of polyglycerol fatty acid ester vesicles. *Journal of Colloid and Interface Science, 327*(2), 446-450. doi:http://doi.org/10.1016/j.jcis.2008.08.047

Duerr-Auster, N., Gunde, R., Mäder, R., & Windhab, E. J. (2009). Binary coalescence of gas bubbles in the presence of a non-ionic surfactant. *Journal of Colloid and Interface Science, 333*(2), 579-584. doi:http://doi.org/10.1016/j.jcis.2009.01.016

Germain, J. C., & Aguilera, J. M. (2014). Multi-scale properties of protein-stabilized foams. *Food Structure, 1*(1), 55-70. doi:https://doi.org/10.1016/j.foostr.2014.01.001

Guo, E., Zeng, G., Kazantsev, D., Rockett, P., Bent, J., Kirkland, M., . . . Lee, P. D. (2017). Synchrotron X-ray tomographic quantification of microstructural evolution in ice cream – a multi-phase soft solid. *RSC Advances, 7*(25), 15561-15573. doi:10.1039/C7RA00642J

Hanselmann, W., & Windhab, E. (1998). Flow characteristics and modelling of foam generation in a continuous rotor/stator mixer. *Journal of Food Engineering, 38*(4), 393-405. doi:http://dx.doi.org/10.1016/S0260-8774(98)00129-0

Indrawati, L., & Narsimhan, G. (2008). Characterization of protein stabilized foam formed in a continuous shear mixing apparatus. *Journal of Food Engineering, 88*(4), 456-465. doi:http://doi.org/10.1016/j.jfoodeng.2008.03.003

Jang, W., Nikolov, A., Wasan, D. T., Chen, K., & Campbell, B. (2005). Prediction of the Bubble Size Distribution during Aeration of Food Products. *Industrial & Engineering Chemistry Research, 44*(5), 1296-1308. doi:10.1021/ie049740x

Kroezen, A. B. J., Groot Wassink, J., & Bertlein, E. (1988). Foam generation in a rotor—stator mixer: schaumerzeugung in einem rotor—stator mischer.

634 *Chemical Engineering and Processing: Process Intensification, 24*(3), 145-
635 156. doi:https://doi.org/10.1016/0255-2701(88)80018-7
636 Kroezen, A. B. J., & Wassink, J. G. (1987). Bubble size distribution and energy
637 dissipation in foam mixers. *Journal of the Society of Dyers and Colourists,*
638 *103*(11), 386-394. doi:10.1111/j.1478-4408.1987.tb01090.x
639 Kulmyrzaev, A., Cancelliere, C., & McClements, D. J. (2000). Characterization of
640 aerated foods using ultrasonic reflectance spectroscopy. *Journal of Food*
641 *Engineering, 46*(4), 235-241. doi:http://doi.org/10.1016/S0260-
642 8774(00)00070-4
643 Lim, K. S., & Barigou, M. (2004). X-ray micro-computed tomography of cellular
644 food products. *Food Research International, 37*(10), 1001-1012.
645 doi:https://doi.org/10.1016/j.foodres.2004.06.010
646 Mary, G., Mezdour, S., Delaplace, G., Lauhon, R., Cuvelier, G., & Ducept, F.
647 (2013). Modelling of the continuous foaming operation by dimensional
648 analysis. *Chemical Engineering Research and Design, 91*(12), 2579-2586.
649 doi:http://doi.org/10.1016/j.cherd.2013.05.020
650 Mezdour, S., Séguineau de Préval, E., Granda, P., Cuvelier, G., & Ducept, F.
651 (2017). *Impact of Interfacial Characteristics on Foam Structure: Study on*
652 *Model Fluids and at Pilot Scale* (Vol. 72).
653 Müller-Fischer, N., Bleuler, H., & Windhab, E. J. (2007a). Dynamically enhanced
654 membrane foaming. *Chemical Engineering Science, 62*(16), 4409-4419.
655 doi:https://doi.org/10.1016/j.ces.2007.05.026
656 Müller-Fischer, N., Suppiger, D., & Windhab, E. J. (2007b). Impact of static
657 pressure and volumetric energy input on the microstructure of food foam
658 whipped in a rotor–stator device. *Journal of Food Engineering, 80*(1), 306-
659 316. doi:http://doi.org/10.1016/j.jfoodeng.2006.05.026
660 Müller-Fischer, N., & Windhab, E. J. (2005). Influence of process parameters on
661 microstructure of food foam whipped in a rotor–stator device within a
662 wide static pressure range. *Colloids and Surfaces A: Physicochemical and*
663 *Engineering Aspects, 263*(1–3), 353-362.
664 doi:http://doi.org/10.1016/j.colsurfa.2004.12.057
665 Narchi, I., Vial, C., Labbafi, M., & Djelveh, G. (2011). Comparative study of the
666 design of continuous aeration equipment for the production of food
667 foams. *Journal of Food Engineering, 102*(2), 105-114.
668 doi:http://doi.org/10.1016/j.jfoodeng.2010.07.030
669 Nicorescu, I., Vial, C., Loisel, C., Riaublanc, A., Djelveh, G., Cuvelier, G., &
670 Legrand, J. (2010). *Influence of protein heat treatment on the continuous*
671 *production of food foams* (Vol. 43).
672 Pugh, R. J. (2016). Generation of bubbles and foams. In R. J. Pugh (Ed.), *Bubble*
673 *and Foam Chemistry* (pp. 155-193). Cambridge: Cambridge University
674 Press.

675 Seguineau De Preval, E., Fabrice, D., Gérard, C., & Samir, M. (2014a). Effect of
676 bulk viscosity and surface tension kinetics on structure of foam generated
677 at the pilot scale. *Food Hydrocolloids, 34*, 104-111.
678 doi:http://doi.org/10.1016/j.foodhyd.2012.12.001
679 Seguineau De Preval, E., Fabrice, D., Gilles, M., Gérard, C., & Samir, M. (2014b).
680 Influence of surface properties and bulk viscosity on bubble size
681 prediction during foaming operation. *Colloids and Surfaces A:*
682 *Physicochemical and Engineering Aspects, 442*, 88-97.
683 doi:http://doi.org/10.1016/j.colsurfa.2013.05.025
684 Tcholakova, S., Lesov, I., Golemanov, K., Denkov, N. D., Judat, S., Engel, R., &
685 Danner, T. (2011). Efficient Emulsification of Viscous Oils at High Drop
686 Volume Fraction. *Langmuir, 27*(24), 14783-14796.
687 doi:10.1021/la203474b
688 Thakur, R. K., Vial, C., & Djelveh, G. (2005). Combined effects of process
689 parameters and composition on foaming of dairy emulsions at low
690 temperature in an agitated column. *Journal of Food Engineering, 68*(3),
691 335-347. doi:https://doi.org/10.1016/j.jfoodeng.2004.06.008
692 Vankova, N., Tcholakova, S., Denkov, N. D., Ivanov, I. B., Vulchev, V. D., &
693 Danner, T. (2007). Emulsification in turbulent flow 1. Mean and maximum
694 drop diameters in inertial and viscous regimes. *J Colloid Interface Sci,*
695 *312*(2), 363-380. doi:10.1016/j.jcis.2007.03.059
696 Walstra, P. (1989). *Principles of Foam Formation and Stability*, London.

697

Table 1. Model fluids composition and properties.

Model fluid	PGE 55 (wt%)	XG (wt%)	Sugar (wt%)	σ_e (mN m^{-1})	η_o (Pa s)	η_∞ (Pa s)	c (-)	m (-)	R^2 (-)
MF1	0.2	0.50	25	39	85	0.009	30.00	0.82	0.993
MF2	0.5	0.50	25	38	116	0.010	33.72	0.83	0.993
MF3	1.0	0.50	25	38	135	0.009	30.00	0.83	0.996
MF4	0.5	0.25	25	38	10	0.010	20.00	0.70	0.992
MF5	0.5	0.35	25	38	35	0.010	28.00	0.75	0.998

Table 2. Geometrical dimensions of continuous rotor-stator device.

Parameter	Symbol (unit)	Value
Diameter of annulus mixing space	L (mm)	5.00
Number of pins on rotor	I (-)	13.00
Number of rotor-stator pairs	h (-)	12.00
Distance between rotor-stator	s (mm)	1.00
Height of rotor/stator pin	q (mm)	2.50
Width of rotor pin	o (mm)	4.70
Rotor diameter	D (mm)	50.00
Distance between rotor pins	z (mm)	12.08

Table 3. Effects of experimental conditions on experimental gas volume fraction (Sample $\emptyset_e$ data shown here for cases where Q_L = 5 L hr^{-1} and Q_G = 5, 7.5 and 10.0 L hr^{-1}).

	MF1		**MF2**			**MF3**		**MF4**		**MF5**	
N **(rpm)**	G/L = 1.0 (τ = 31 s)	G/L = 1.5 (τ = 25 s)	G/L = 1.0 (τ = 31 s)	G/L = 1.5 (τ = 25 s)	G/L = 2.0 (τ = 20 s)	G/L = 1.0 (τ = 31 s)	G/L = 1.5 (τ = 25 s)	G/L = 1.0 (τ = 31 s)	G/L = 1.5 (τ = 25 s)	G/L = 1.0 (τ = 31 s)	G/L = 1.5 (τ = 25 s)
500	0.52	blow-by	0.52	0.62	blow-by	0.51	0.61	0.51	0.61	0.52	0.62
750	0.53	blow-by	0.52	0.63	blow-by	0.51	0.61	0.52	0.61	0.52	0.62
1000	0.53	0.63	0.52	0.63	0.69	0.51	0.61	0.51	0.61	0.52	0.62
1250	0.53	0.63	0.52	0.63	0.69	0.52	0.61	0.52	0.61	0.52	0.62
1500	0.54	0.63	0.52	0.63	0.69	0.53	0.61	0.52	0.62	0.53	0.63
1750	0.54	0.63	0.52	0.63	0.69	0.53	0.61	0.53	0.62	0.52	0.63

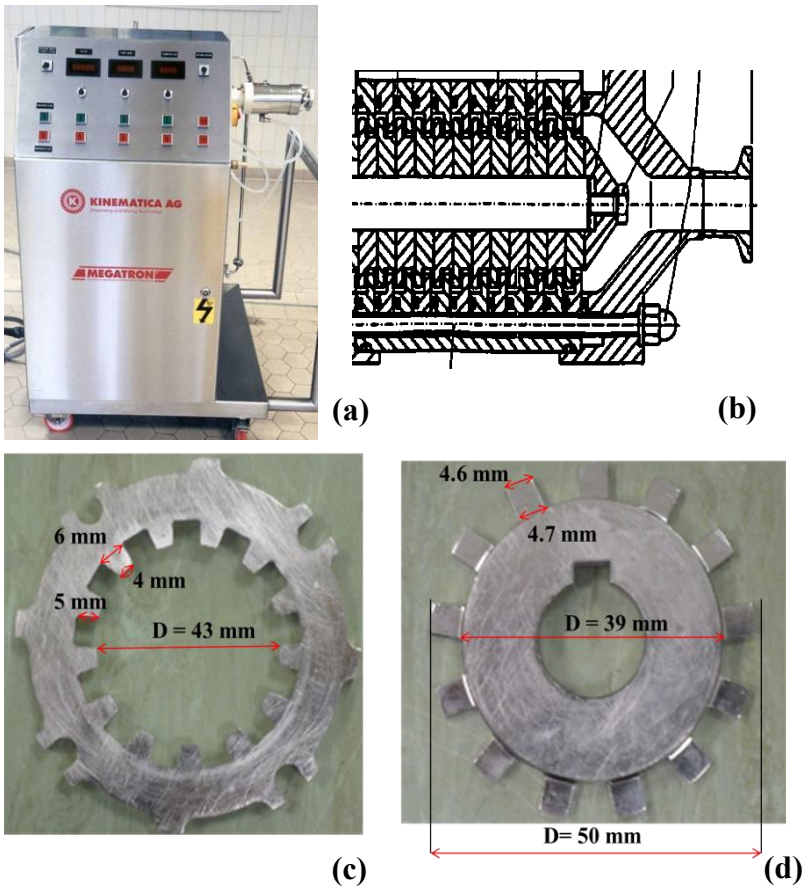

Fig. 1. Foam generator: (a) pilot-scale continuous rotor-stator unit; (b) schematic of mixing-head chamber; (c) stator; (d) rotor.

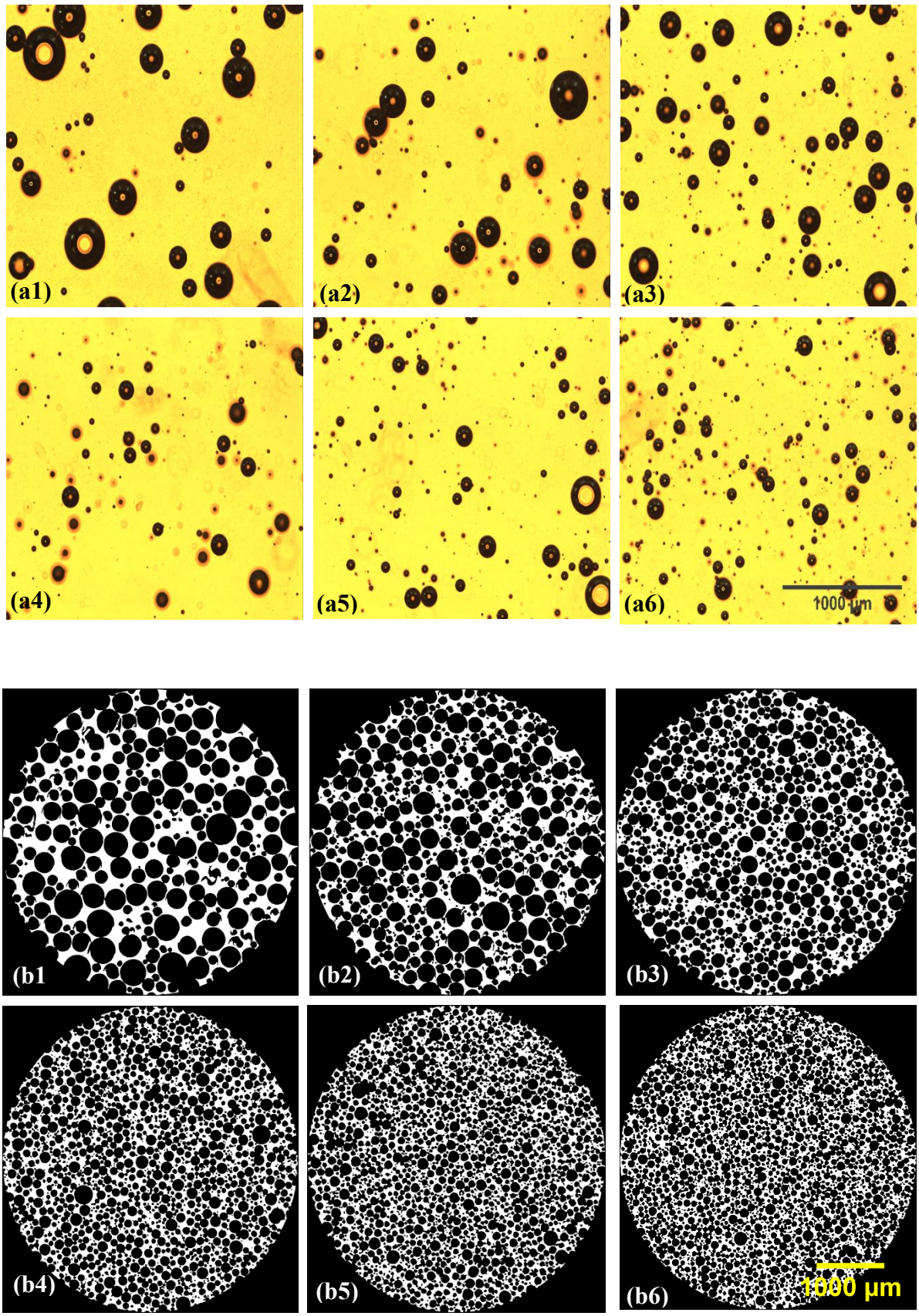

Fig. 2. Foam images obtained using: a digital microscope (a1-a6); and X-ray micro-CT technique (2D slices) (b1-b6). Fluid MF2; G/L = 1.5; N = 500, 750, 1000, 1250, 1500, 1750 rpm, respectively.

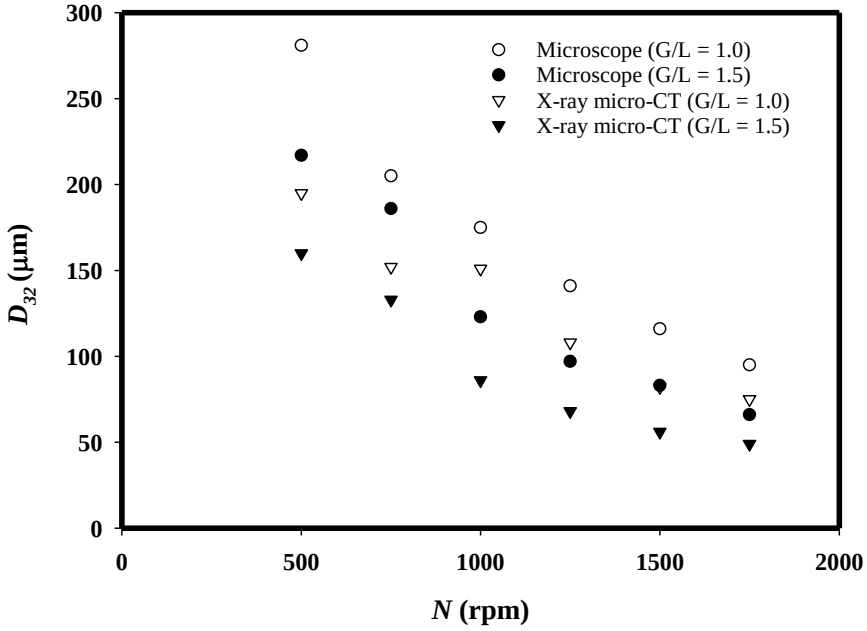

Fig. 3. Comparison of D_{32} obtained from light microscopy and X-ray micro-CT techniques for MF2.

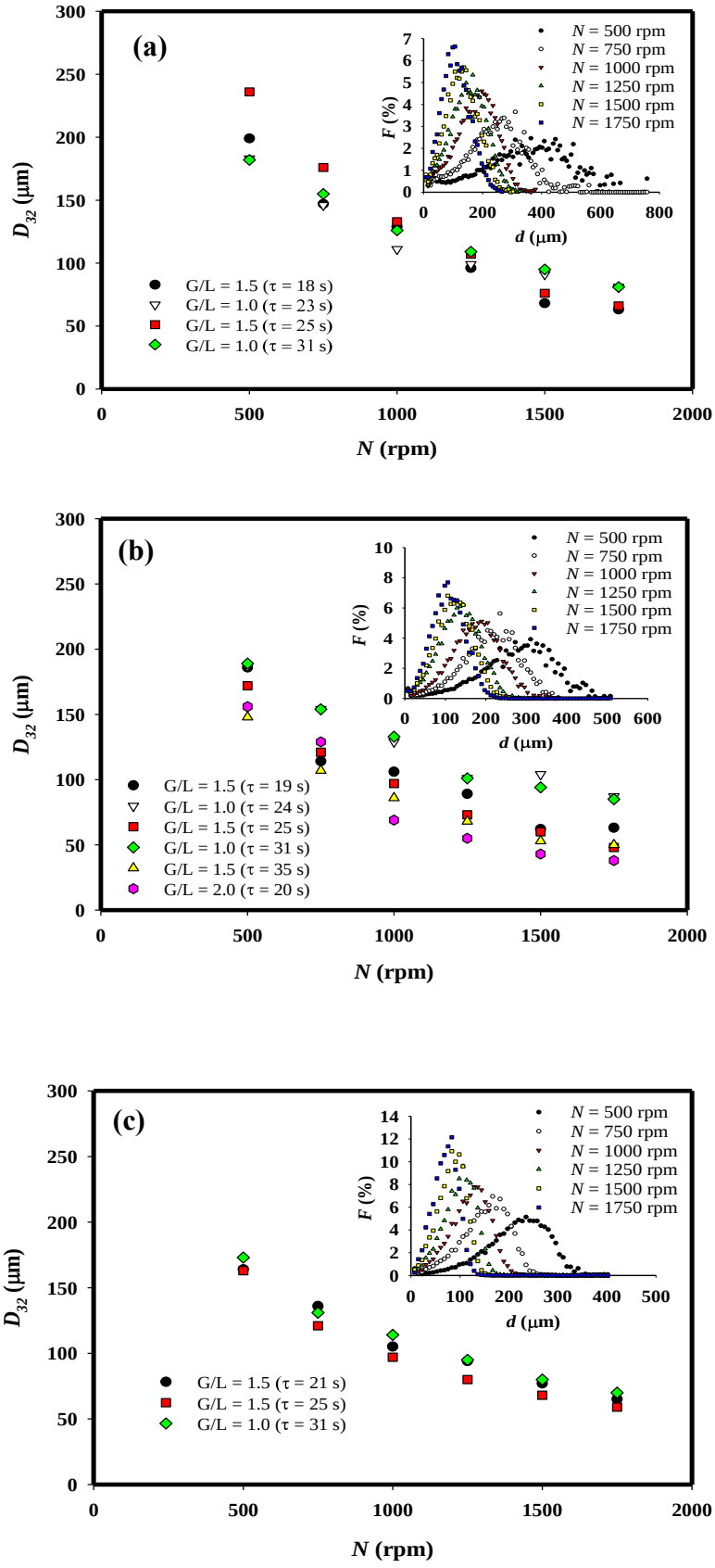

Fig. 4. Effects of rotational speed and G/L ratio on D_{32}: **(a)** MF1; **(b)** MF2; and **(c)** MF3.

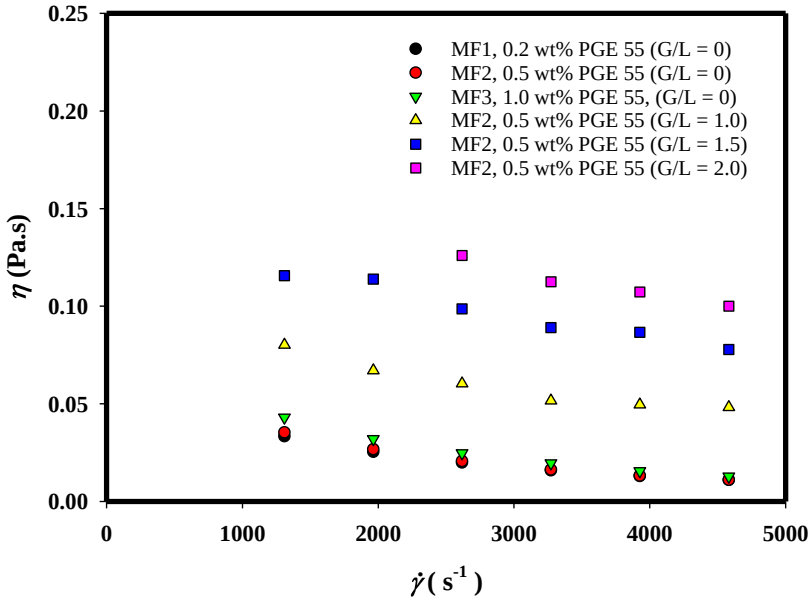

Fig. 5. Variation of apparent viscosity (Eq. 1) of gas-liquid dispersion inside mixing-head chamber and of model fluids under the same process conditions of shear (Eq. 11).

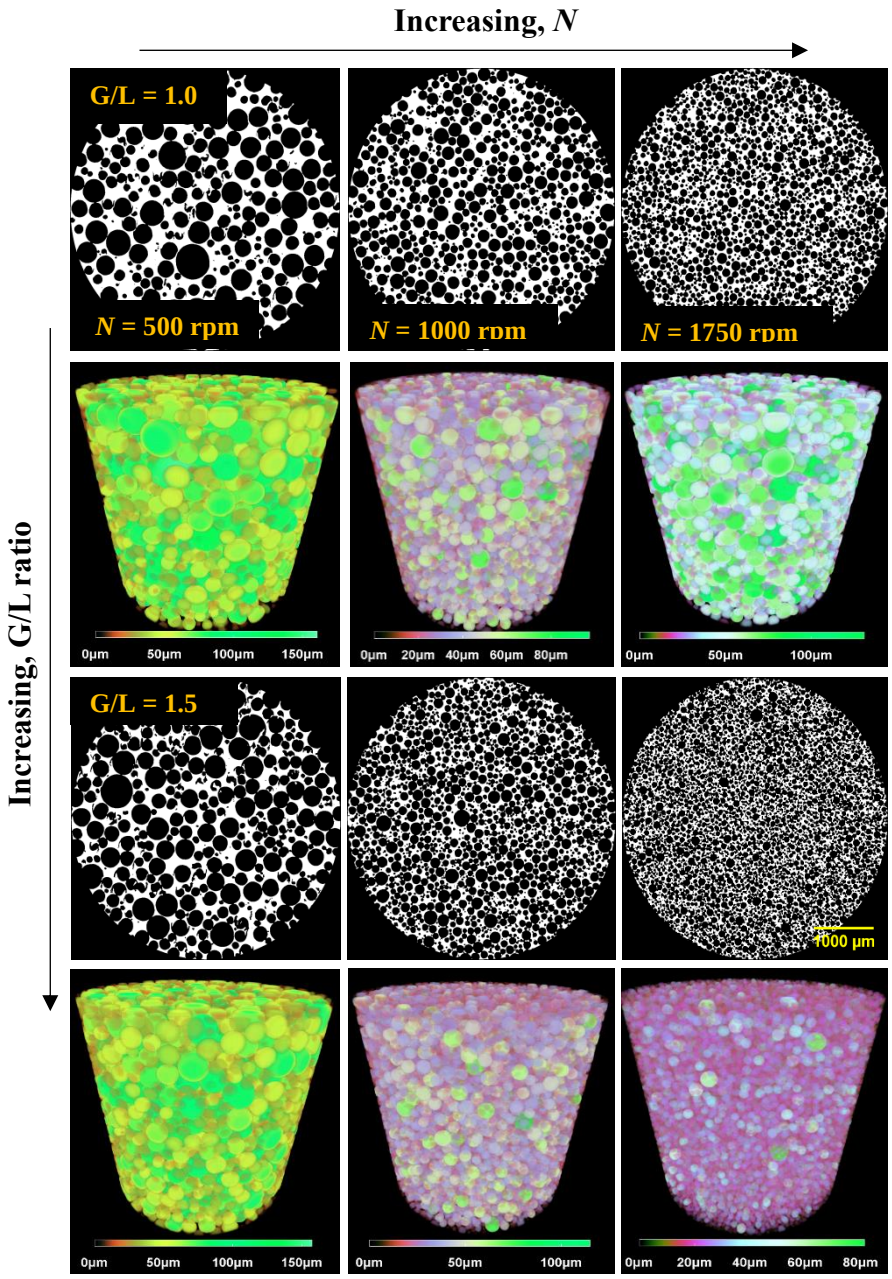

Fig. 6. Rendered 3D X-ray micro-CT model of foam generated from MF2 numerically cut to reveal its inner structure.

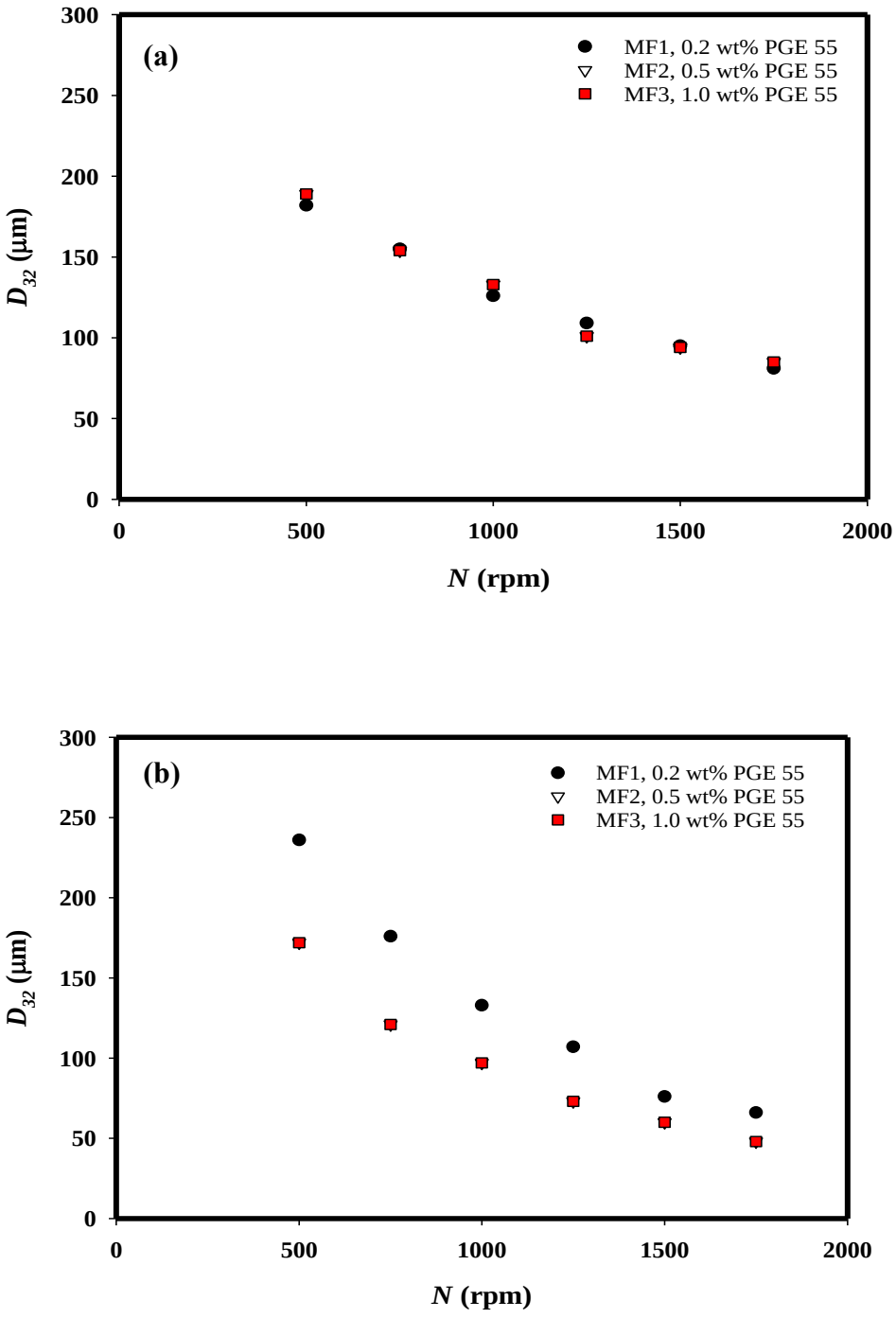

Fig. 7. Effects of surfactant concentration on D_{32}: (a) G/L = 1.0; (b) G/L = 1.5.

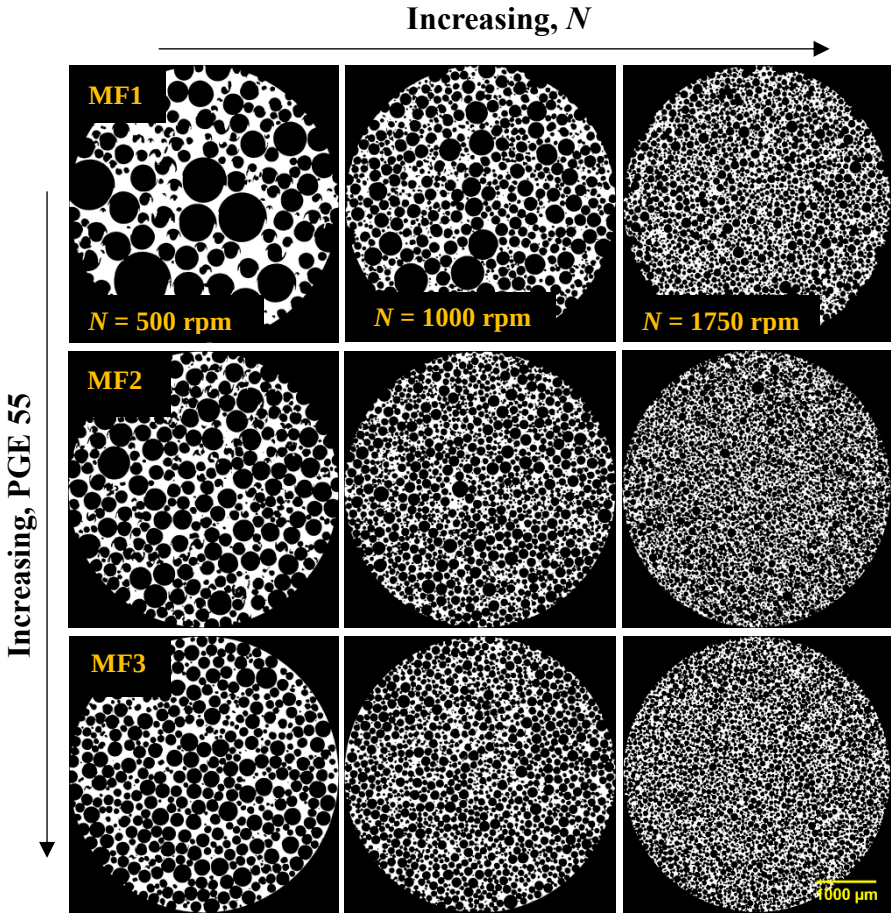

Fig. 8. X-ray micro-CT images of foam samples generated from MF1, MF2 and MF3 at G/L = 1.5.

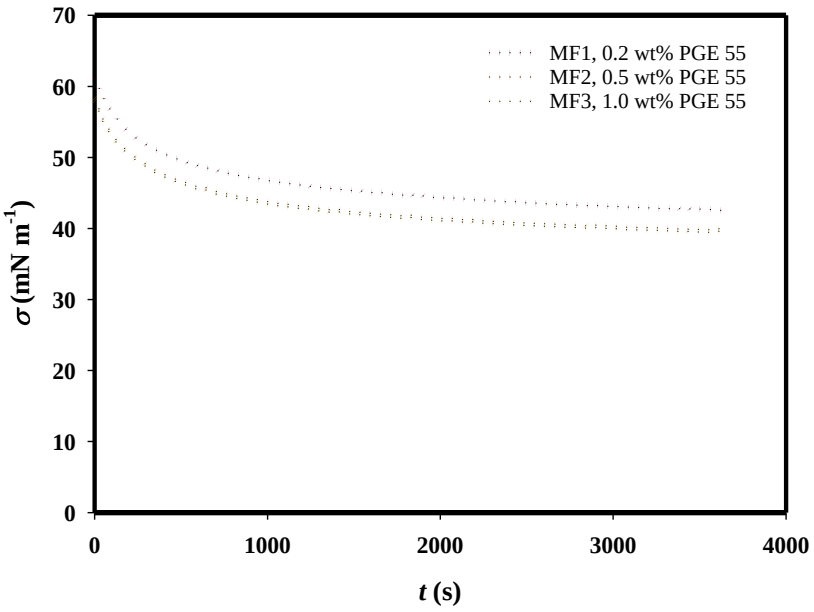

Fig. 9. Dynamics surface tension isotherm of model fluids.

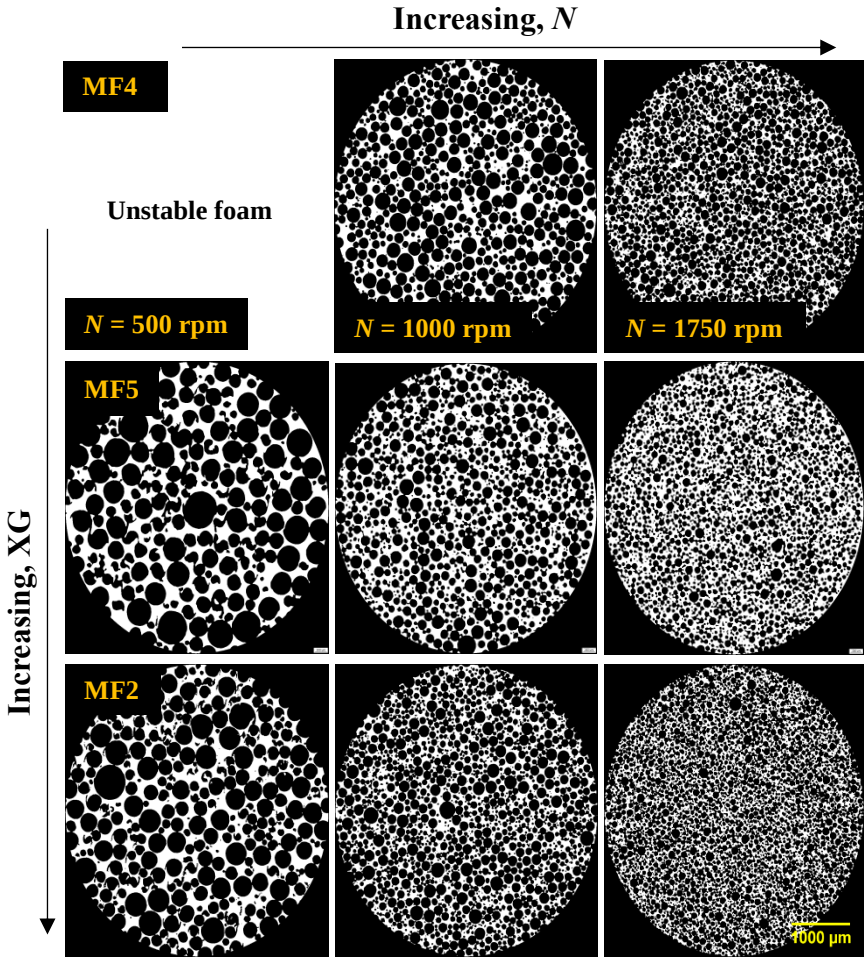

Fig. 10. X-ray micro-CT images of foam samples generated from MF2, MF4 and MF5 at G/L = 1.5.

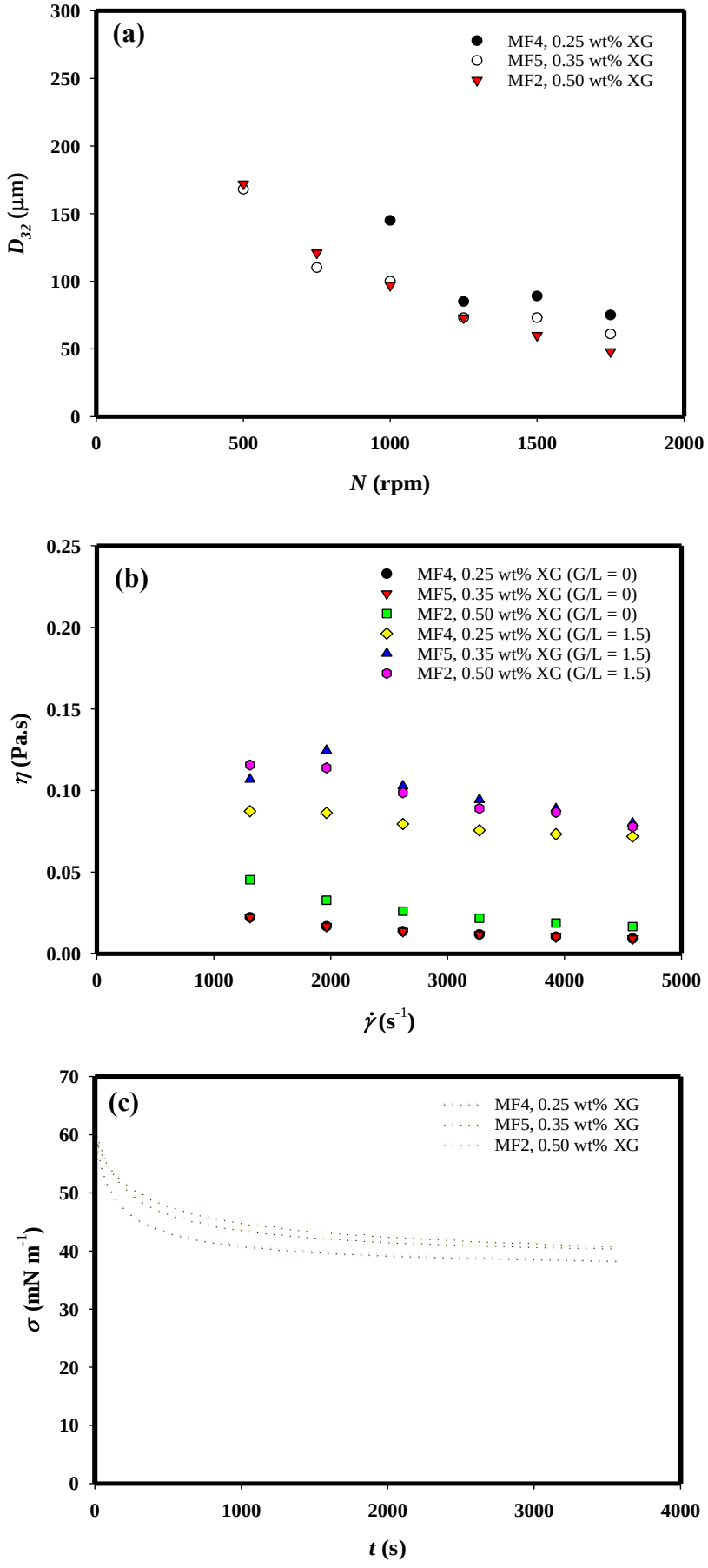

Fig. 11. Effects of Xanthan gum concentration: (a) mean bubble size; (b) dynamic surface tension; (c) apparent dispersion viscosity.

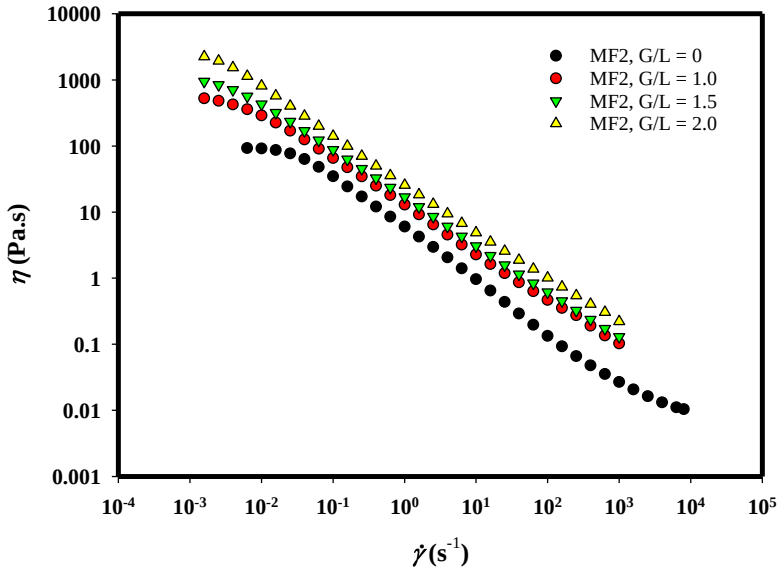

Fig. 12. Typical apparent viscosity curves of fluid MF2 and associated foam generated at N = 1000 rpm and different G/L ratios.

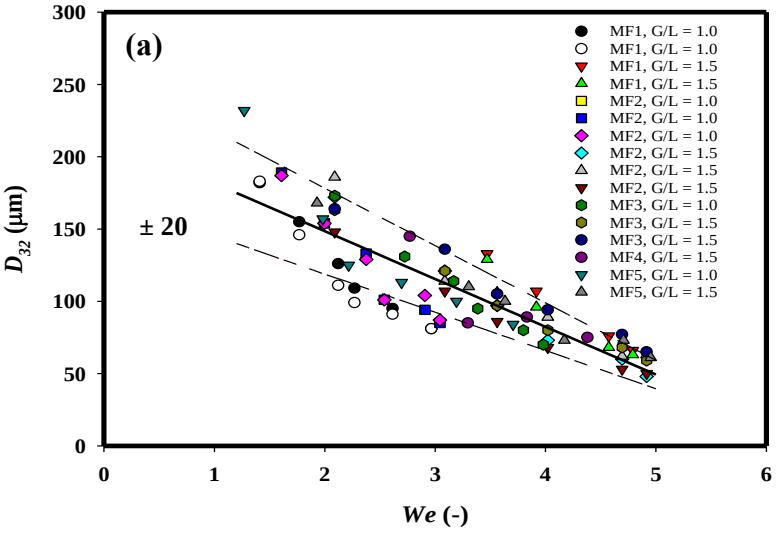

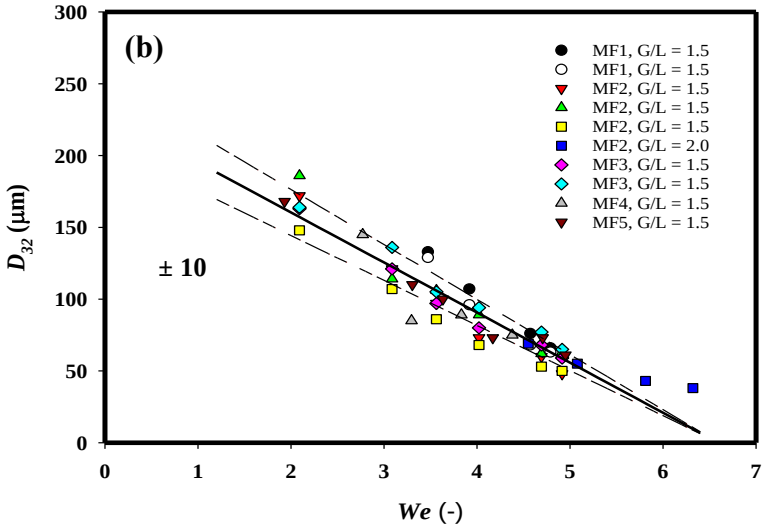

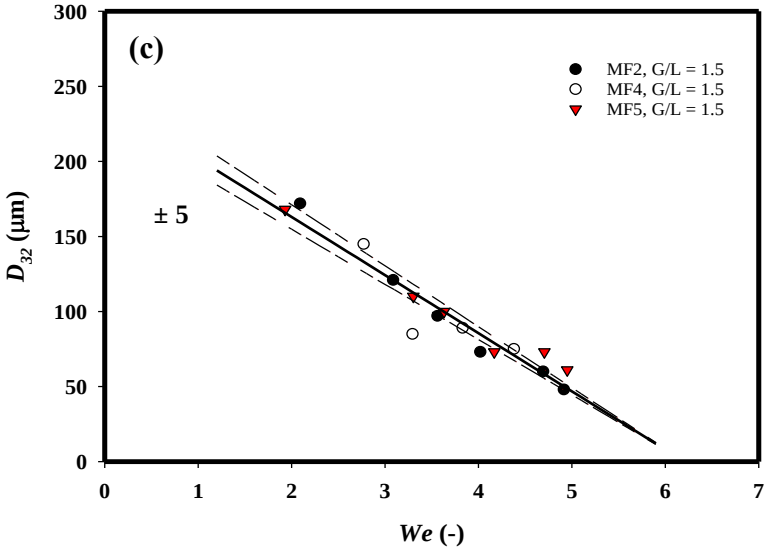

Fig. 13. Variation D_{32} as a function of *We* for: (a) MF1 – MF5 at G/L = 1.0 – 2.0; (b) MF1 – MF5 at G/L = 1.5, 2.0; (c) MF2, MF4 and MF5 at G/L = 1.5.

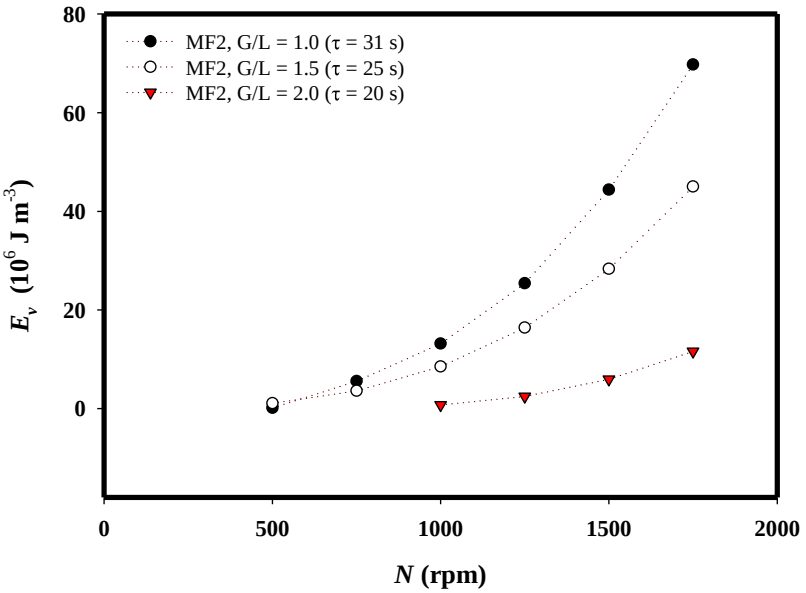

Fig. 14. Effects of rotor speed and G/L ratio on net volumetric energy input

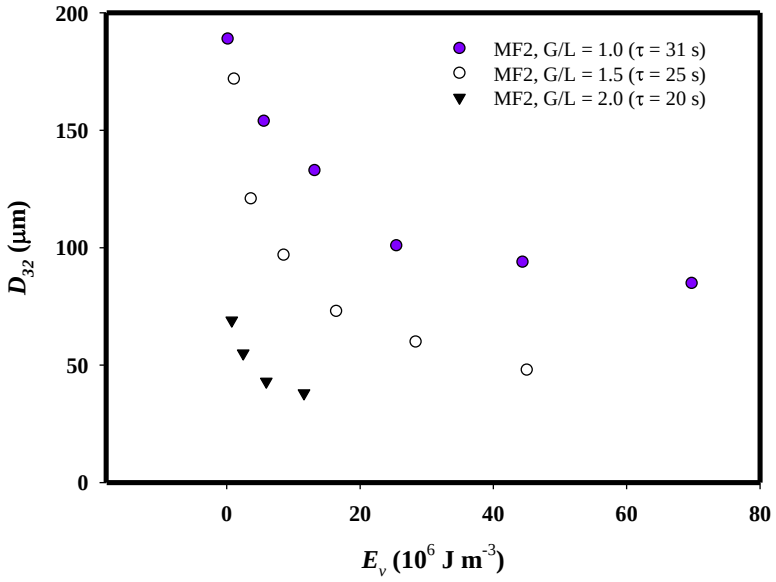

Fig. 15. Variation of D_{32} as a function of E_v.

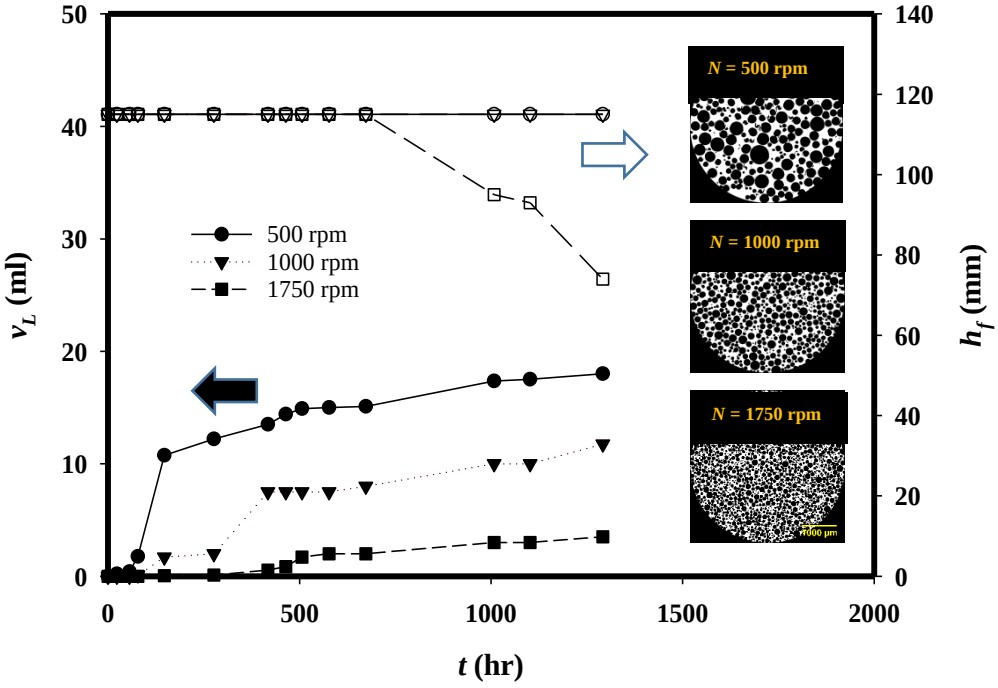

Fig. 16. Typical profiles of foam drainage and collapse for MF2 foams at G/L = 1.0 (filled symbols refer to liquid drainage and open symbols refer to foam collapse).

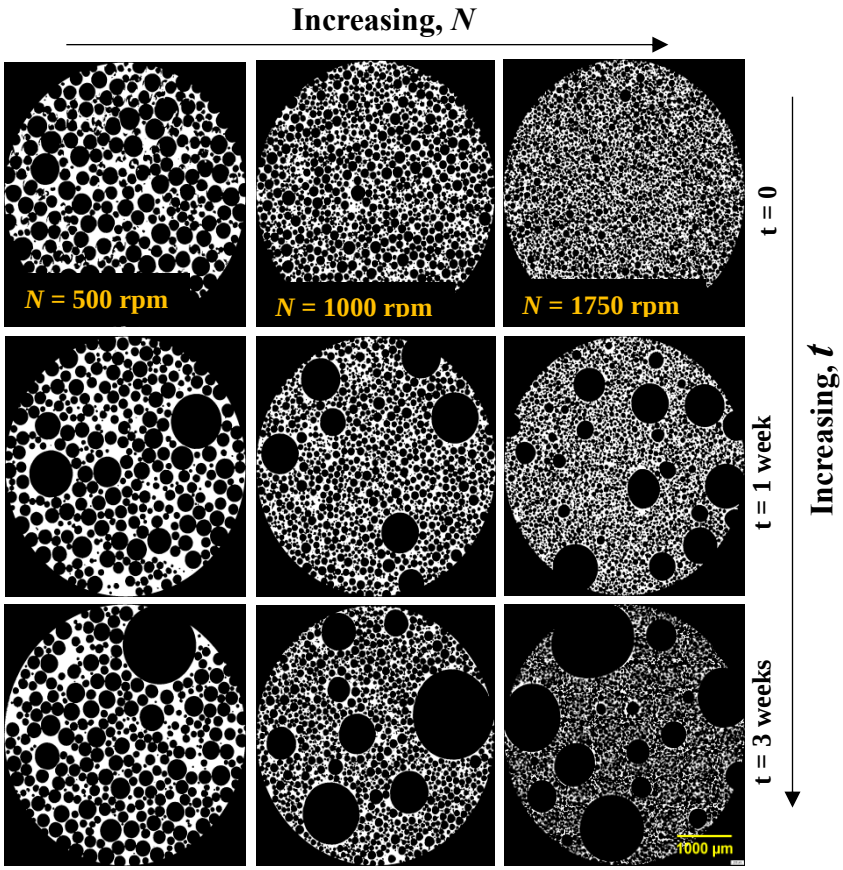

Fig. 17. Typical coarsening X-ray micro-CT images of MF2 foams at G/L = 1.5.